



**Titre:** An eight-channel Tx dipole and 20-channel Rx loop coil array for MRI of the cervical spinal cord at 7 tesla

**Auteurs:** Nibardo Lopez Rios, Kyle M. Gilbert, Daniel S. Papp, Gaspard Cereza, Alexandru Foias, Deshpande Rangaprakash, Markus W. May, Bastien Guerin, Lawrence L. Wald, Boris Keil, Jason P. Stockmann, Robert Barry, & Julien Cohen-Adad

**Date:** 2023

**Type:** Article de revue / Article


**Référence:** Rios, N. L., Gilbert, K. M., Papp, D. S., Cereza, G., Foias, A., Rangaprakash, D., May, M. W., Guerin, B., Wald, L. L., Keil, B., Stockmann, J. P., Barry, R., & Cohen-Adad, J. (2023). An eight-channel Tx dipole and 20-channel Rx loop coil array for MRI of the cervical spinal cord at 7 tesla. *NMR in Biomedicine*, 36(11), e5002 (17 pages). <https://doi.org/10.1002/nbm.5002>

 **Document en libre accès dans PolyPublie**  
Open Access document in PolyPublie

**URL de PolyPublie:** <https://publications.polymtl.ca/54363/>

**Version:** Version officielle de l'éditeur / Published version  
Révisé par les pairs / Refereed

**Conditions d'utilisation:** CC BY-NC-ND  
Terms of Use:

 **Document publié chez l'éditeur officiel**  
Document issued by the official publisher

**Titre de la revue:** NMR in Biomedicine (vol. 36, no. 11)  
Journal Title:



**Maison d'édition:** Wiley  
Publisher:

**URL officiel:** <https://doi.org/10.1002/nbm.5002>  
Official URL:

**Mention légale:** This is an open access article under the terms of the Creative Commons Attribution-NonCommercial-NoDerivs License, which permits use and distribution in any medium, provided the original work is properly cited, the use is non-commercial and no modifications or adaptations are made.  
Legal notice:

## RESEARCH ARTICLE

# An 8-channel Tx dipole and 20-channel Rx loop coil array for MRI of the cervical spinal cord at 7 Tesla

Nibardo Lopez-Rios<sup>1</sup>  | Kyle M. Gilbert<sup>2</sup> | Daniel Papp<sup>1</sup>  | Gaspard Cereza<sup>1</sup> |  
Alexandru Foias<sup>1</sup> | Deshpande Rangaprakash<sup>3,4</sup> | Markus W. May<sup>5,6</sup> |  
Bastien Guerin<sup>3,4</sup> | Lawrence L. Wald<sup>3,4,7</sup> | Boris Keil<sup>8,9</sup> | Jason P. Stockmann<sup>3,4</sup> |  
Robert L. Barry<sup>3,4,7</sup> | Julien Cohen-Adad<sup>1,10,11,12</sup>

<sup>1</sup>NeuroPoly Lab, Institute of Biomedical Engineering, Polytechnique Montréal, Montréal, Québec, Canada

<sup>2</sup>Centre for Functional and Metabolic Mapping, The University of Western Ontario, London, Ontario, Canada

<sup>3</sup>Athinoula A. Martinos Center for Biomedical Imaging, Department of Radiology, Massachusetts General Hospital, Charlestown, Massachusetts, USA

<sup>4</sup>Harvard Medical School, Boston, Massachusetts, USA

<sup>5</sup>Erwin L. Hahn Institute for Magnetic Resonance Imaging, University of Duisburg-Essen, Essen, Germany

<sup>6</sup>High Field and Hybrid MR Imaging, University Hospital Essen, University of Duisburg-Essen, Essen, Germany

<sup>7</sup>Harvard-Massachusetts Institute of Technology Health Sciences and Technology, Cambridge, Massachusetts, USA

<sup>8</sup>Institute of Medical Physics and Radiation Protection, University of Applied Sciences Mittelhessen, Giessen, Germany

<sup>9</sup>Department of Diagnostic and Interventional Radiology, University Hospital Marburg, Philipps University of Marburg, Marburg, Germany

<sup>10</sup>Functional Neuroimaging Unit, CRIUGM, Université de Montréal, Montréal, Québec, Canada

<sup>11</sup>Mila - Quebec AI Institute, Montréal, Québec, Canada

<sup>12</sup>Centre de recherche du CHU Sainte-Justine, Université de Montréal, Montréal, Québec, Canada

## Correspondence

Nibardo Lopez-Rios, NeuroPoly Lab, Institute of Biomedical Engineering, Polytechnique Montréal, 2900 Edouard-Montpetit Boulevard, H3T1J4, Montréal, Québec, Canada.  
Email: [nibardo.lopez-rios@polymtl.ca](mailto:nibardo.lopez-rios@polymtl.ca)

## Funding information

JCA received financial support from the Canada Research Chair in Quantitative Magnetic Resonance Imaging (CRC-2020-00179), the Canadian Institute of Health Research (CIHR FDN-143263), the Canada Foundation for Innovation (32454, 34824), the Fonds de Recherche du Québec - Santé (322736), the Natural Sciences and Engineering Research Council of Canada (RGPIN-2019-07244), the Canada First Research Excellence Fund (IVADO and TransMedTech), the Quebec BioImaging

## Abstract

The quality of cervical spinal cord images can be improved by the use of tailored radiofrequency (RF) coil solutions for ultrahigh field imaging; however, very few commercial and research 7-T RF coils currently exist for the spinal cord, and in particular, those with parallel transmission (pTx) capabilities. This work presents the design, testing, and validation of a pTx/Rx coil for the human neck and cervical/upper thoracic spinal cord. The pTx portion is composed of eight dipoles to ensure high homogeneity over this large region of the spinal cord. The Rx portion is made up of twenty semiadaptable overlapping loops to produce high signal-to-noise ratio (SNR) across the patient population. The coil housing is designed to facilitate patient positioning and comfort, while also being tight fitting to ensure high sensitivity. We demonstrate RF shimming capabilities to optimize  $B_1^+$  uniformity, power efficiency, and/or specific absorption rate efficiency.  $B_1^+$  homogeneity, SNR, and g-factor were

**Abbreviations:** BW, bandwidth; CAD, computer-aided design; CoV, coefficient of variation; CP, circularly polarized; FA, flip angle; FLASH, fast low-angle shot; FOV, field of view; GRE, gradient echo; INV2, second inversion time; MP2RAGE, magnetization prepared 2 rapid acquisition gradient echo; MR, magnetic resonance; MRI, magnetic resonance imaging; pTx, parallel transmission; RF, radiofrequency; ROI, region of interest; Rx, receive; SAR, specific absorption rate; SC, spinal cord; SNR, signal-to-noise ratio; TE, echo time; TEM, transverse electromagnetic; TR, repetition time; Tx, transmit; VNA, vector network analyzer; VOPs, virtual observation points.

This is an open access article under the terms of the [Creative Commons Attribution-NonCommercial-NoDerivs](https://creativecommons.org/licenses/by-nc-nd/4.0/) License, which permits use and distribution in any medium, provided the original work is properly cited, the use is non-commercial and no modifications or adaptations are made.

© 2023 The Authors. *NMR in Biomedicine* published by John Wiley & Sons Ltd.

Network (5886, 35450), and Mila - Tech Transfer Funding Program. KMG received financial support from the Canada Foundation for Innovation, Canada First Research Excellence Fund to BrainsCAN, and Brain Canada Platform Support Grant. Imaging performed at the Athinoula A. Martinos Center for Biomedical Imaging used funds from Biotechnology Resource Grants provided by the National Institute of Biomedical Imaging and Bioengineering, National Institutes of Health (NIH) to the Center for Functional Neuroimaging Technologies (P41EB015896), the Center for Mesoscale Mapping (P41EB030006), and RLB (R01EB027779). Also, LLW received support from the Office of the Director of the NIH (S10OD023637).

[Correction added on 21 July 2023, after first online publication: the article title has been corrected in this version.]

evaluated in adult volunteers and demonstrated excellent performance from the occipital lobe down to the T4-T5 level. We compared the proposed coil with two state-of-the-art head and head/neck coils, confirming its superiority in the cervical and upper thoracic regions of the spinal cord. This coil solution therefore provides a convincing platform for producing the high image quality necessary for clinical and research scanning of the upper spinal cord.

#### KEYWORDS

7 T, dipole, MRI, radiofrequency coil, spinal cord, transmit/receive coil, ultrahigh field

## 1 | INTRODUCTION

Clinical and research magnetic resonance imaging (MRI) studies of the cervical spinal cord can benefit significantly from the increased signal-to-noise ratio (SNR) and contrasts resulting from the recent developments in ultrahigh fields. The high resolution achieved, particularly at 7 T, has great potential for enhanced structural, functional, quantitative, and spectroscopic studies of the small structures that comprise this region.<sup>1,2</sup> The anatomical characteristics of the spinal cord present a challenge for MRI radiofrequency (RF) coils to produce both a uniform transmit field and a high receive sensitivity at 7 T. The confluence of the large inferior–superior dimension of the spinal cord, its dissimilar curvature and posterior location, and the variance in surrounding body circumference along its longitudinal axis, has inspired the development of a wide range of tailored solutions for different sections of the spine.

Overall, spine coil transceiver archetypes can be classified based upon the anatomical region to which they are tailored: head–neck, cervical spine, thoracic, and lumbar. Head–neck coils,<sup>3–5</sup> as well as cervical spine coils,<sup>2,6</sup> are typically conformed to the complex shape of these sections of anatomy: the focal coverage produces higher transmit efficiency and receive sensitivity. Imaging of the thoracic and lumbar regions requires enlarged coverage in the superior–inferior direction, which has been accomplished with planar arrays residing posterior to the subject.<sup>7–11</sup> Torso coils are also used for these two regions, being either rigid<sup>12</sup> or made flexible<sup>13–15</sup> to contend with the variance in body size between subjects. In a select number of institutions, whole-body coils have been developed<sup>16,17</sup> that reside outside the bore liner: this engineering feat would allow for imaging of the entire spine.

There exists a dearth in the literature for coils tailored to an imaging region spanning from the occipital lobe to the midthoracic, a region probed for the detection of multiple sclerosis lesions.<sup>18</sup> The disparate requirements for conforming the receive coil to the vastly different size and shape of the neck versus the upper torso must be accommodated to optimize sensitivity: a tailoring of the receive-coil geometry to this anatomy is therefore imperative. Conversely, a transmit coil must be sufficiently distant from the body to produce a uniform field, yet not so distant as to produce inadequate efficiency for attaining the required RF pulses (a common challenge for 7-T spine coils), and this all must be achieved while avoiding the geometric impediments of the shoulders and the receive coil.

At 7 T, spine coils have accomplished these tasks with either transceiver arrays<sup>4,10,11</sup> or by separating transmit and receive functions into disparate coils.<sup>2,3,5–7,16,19,20</sup> This latter approach often permits a greater number of receive elements to be employed, and as such was chosen as the topology for the current study.

Receive arrays must be both highly sensitive and have the requisite geometrical layout to reduce noise amplification during the reconstruction of accelerated images.<sup>21,22</sup> Various challenges must be overcome during the design of a receive coil for the target region of interest (ROI), some of which are specific to high-field imaging. Among these confounds is the location of the spinal cord, where the SNR exhibited by existing arrays is normally reduced.<sup>23,24</sup> The spinal cord's depth varies along its length, a challenge that is exacerbated by the variability of the human anatomy when designing a coil to accommodate a large portion of the population. Consequently, to maximize signal sensitivity, it is advantageous to minimize the distance between receive elements and the spine. This results in coil elements being distributed over a complex surface, with a high density of elements proximal to the neck (thereby increasing coupling between elements) and a low density in the upper thorax, including no coverage around the shoulders (causing a signal reduction). In this regard, adjustable designs<sup>25</sup> can be beneficial, despite their increase in design complexity. Likewise, the array can be physically split to facilitate accommodation of the subject and to reduce stress during scanning. The resultant complexity in the coil former leads to a more difficult decoupling process due to the diversity of the element dimensions and layouts. Furthermore, the proximity and geometry of the transmit coil must be considered to determine the location of the preamplifiers and receive-coil cabling that limits transmit–receive interaction.

Transmit coils are responsible for creating transverse magnetic fields ( $B_1^+$ ) that are uniform, power efficient and specific absorption rate (SAR) efficient, challenges exacerbated at high field strengths due to the reduced wavelength within the human body and the resultant complex wave behavior.<sup>26,27</sup> Improvements in  $B_1^+$  uniformity,<sup>28,29</sup> required to mitigate spatially dependent tissue contrast, have been addressed through the advent of parallel-transmit coils<sup>30,31</sup> augmented with RF shimming<sup>32,33</sup> and spatially selective RF pulses.<sup>34</sup> Power efficiency must only be sufficient to produce the requisite RF pulses within the constraints imposed by the RF power amplifiers; therefore, the more salient performance metric at high field is SAR efficiency, as local SAR is often the practical limitation when creating pulse-sequence protocols.

For spinal cord imaging at ultrahigh field, various design topologies have been developed for transmit coils. Achieving sufficient transmit efficiency in the spinal cord—a relatively deep structure—can prove challenging. Local transmit coils can reduce this difficulty by placing the coil in close proximity to the subject. This has been accomplished with two-channel coils<sup>7,35–37</sup> and array coils.<sup>2,5,8,20,38–40</sup> To additionally leverage the capability of array coils to improve transmit uniformity through RF shimming or spatially selective pulses, an eight-channel transverse electromagnetic (TEM) coil<sup>17</sup> and a 16-channel meandered stripline coil<sup>41</sup> were developed for torso imaging, including the lower spinal cord. A more general solution for whole-body imaging has been to build the transmit coil into the bore liner: these have included a TEM coil<sup>17</sup> and 32-channel stripline array.<sup>42</sup> The latter solution combined the capacity of a large-diameter, high-density transmit coil (to improve uniformity) with a custom power amplifier for each transmitter near the magnet, thereby compensating for the commensurate reduction in efficiency.

Recently, because it is an efficient high-frequency radiator, the dipole has been introduced as a constituent element for ultrahigh-field transmit coils,<sup>43–46</sup> thereby improving efficiency in deep tissues, while commensurately reducing SAR.<sup>47,48</sup> As such, dipoles have been used as the building block for transmit coils intended for head imaging<sup>49–52</sup> and body imaging.<sup>15,53</sup> For spine imaging, dipoles have been implemented to improve transmit efficiency,<sup>7,12,39</sup> SAR efficiency,<sup>19,54</sup> and to increase the potential field of view (FOV).<sup>36</sup>

In this work, we present a single-housing transmit/receive coil, composed of eight geometrically adapted Tx dipoles and 20 anatomically shaped Rx loops, for an extended FOV spanning from the occipital lobe to the upper thoracic spine (T4–T5). The coil features an adjustable anterior section that facilitates the positioning of subjects and allows the Rx array to be adapted to them. The coil was validated by simulations, on the workbench and in the scanner, with multiple subjects of variable morphologies. RF shimming was demonstrated with the multichannel Tx design to further improve the  $B_1^+$  uniformity, power efficiency, or SAR efficiency. The coil was compared with a commercially available coil and a recently developed head–neck coil.<sup>5</sup>

## 2 | METHODS

### 2.1 | Coil construction and evaluation on the bench

The Tx and the Rx coils were mounted on a single structure with a fixed posterior section and a hinged anterior section to expedite the setup and removal of subjects (Figure 1A,B). Fifteen receive elements were mounted on the close-fitting, 3-mm-thick inner surface of the posterior

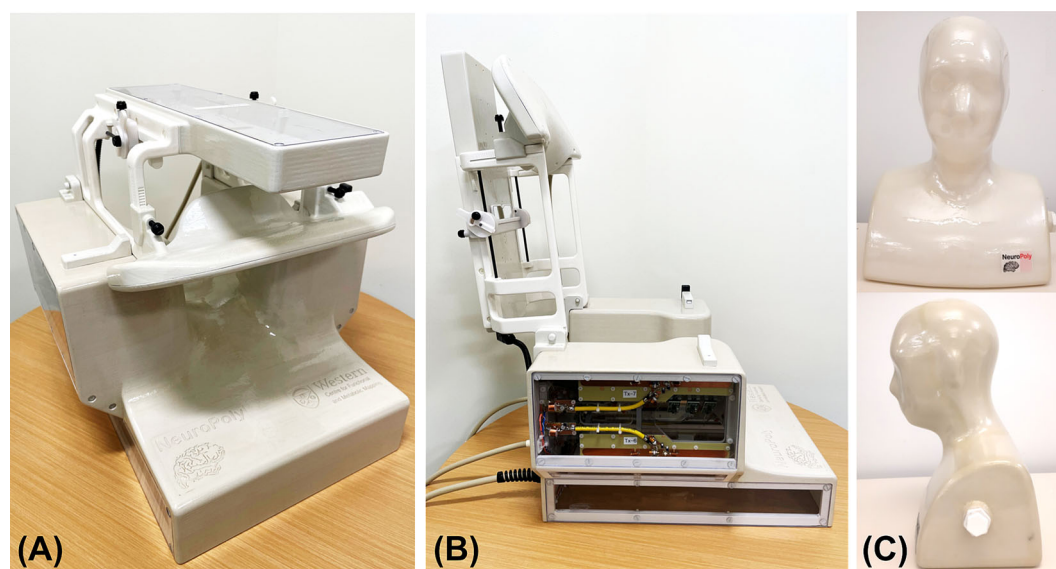


**FIGURE 1** Views of the assembled Tx/Rx coil in (A) Its imaging mode, and (B) With the hinged assembly (Tx-8/Rx-16 to 20) completely open to allow subject placement. (C) The head–neck phantom built for coil adjustment and evaluation.

section to produce high signal sensitivity. In this fixed section, transmit elements Tx-1 to 7 were installed on machined polycarbonate sheets: three posterior, and two each on the left and right sides. Tx-8 and Rx-16 to 20 were placed on the anterior section. These five receive elements comprise a functionally independent assembly whose distance to the subject can be manually adjusted by the MR technologist, or ultimately detached, allowing the coil to be adapted to an extended population. The anterior section is locked in place during scanning to prevent movement. External cabling enters the posterior section of the coil and cannot be in direct contact with the subject during scans. The cable of the Tx-8 element was externally routed from the fixed to the hinged section and protected with cable wrap. A mirror, with adjustable Z-axis position and tilt angle, was integrated underneath the anterior transmit housing to reduce patient anxiety and to allow for the presentation of visual stimuli. Open spaces around the face of the subject were maximized to further reduce claustrophobia. The design files for this coil are available at: <https://github.com/neuropoly/coil-spine7t>. A head-neck phantom (Figure 1C) was also built to adjust and evaluate the coil.

### 2.1.1 | Receive coil

We used a computer-aided design tool (Autodesk, AutoCAD, version 2018, San Francisco, CA, USA) to design a close-fitting inner coil former. As a reference for this process, we utilized a three-dimensional (3D) average head model created by a procedure described in an earlier work.<sup>55</sup> The basic structure of the resulting former was a complex surface that slightly reduced the typical curvature of the cervical spine during scans, while leaving additional space for padding. The anterior of this surface was modified from the average head model to facilitate its adaptability to the highly variable anatomy of that region over the population. Based on the 3D probabilistic localization of the spinal cord obtained with the procedure cited above, we determined that 20 circular loops placed directly on this surface could image the entire ROI with an adequate sensitivity (Figure 2A,C). The loops located in the fixed section (Rx-1 to 15) were proximal to the posterior and lateral portions of the neck, while extending from the occipital to the midthoracic regions. The remaining loops (Rx-16 to 20) were intended to improve the overall sensitivity of the coil on the anterior portion of the neck and the upper chest, especially in the inferior aspect of the ROI, where the distribution of the posterior 15 receive elements was less dense.

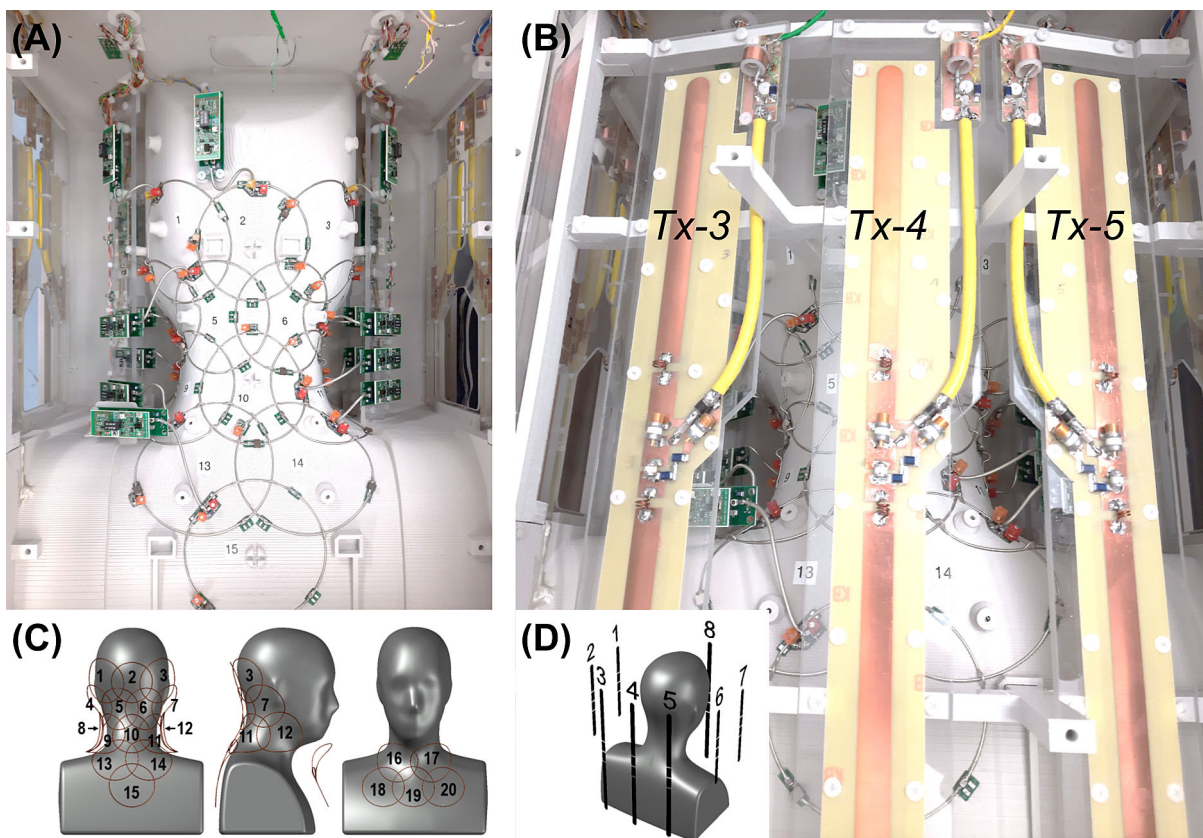


**FIGURE 2** Posterior views of the coil and element layout. (A) Rx subarray comprising elements 1 to 15; lateral Tx elements can be seen on the sides: 1, 2 on the left and 6, 7 on the right. (B) Full view of Tx elements 3, 4, and 5. (C) Distribution of Rx loops on the posterior (1–15) and anterior (16–20) Rx coil sections. (D) Posterior-right perspective view of the phantom showing the arrangement of Tx dipoles.

The receive-loop contours were generated in CST Studio Suite (Waltham, MA, USA) using the previously designed coil sections imported from AutoCAD. To do this, spheres were sequentially created and intersected with the former sections. The lines defining the intersections between the former sections and the spheres were converted into wires ( $r = 0.64$  mm), resulting in circular loops. Each loop was segmented into four sections of approximately equal length, creating four gaps where simulation ports were connected. Tuning and matching of the loops were performed by co-simulation after assigning variable components to the simulation ports. The loops were tuned, and the output impedance was adjusted to  $50 \Omega$ . Components used for preamp decoupling were not included in these simulations. Coupling between adjacent pairs was minimized by adjusting the positions and diameters of the corresponding spheres. The final sphere diameters were between 88 and 98 mm. The symmetry of the coil was leveraged to significantly reduce the number of iterations. Lastly, the sensitivity profile of the complete array was estimated by computing and combining individual  $B_1^-$  maps.

The final array structure was exported back to AutoCAD and subtracted from the original coil formers. This operation generated grooves that were used as a guide to lay the loops. Loops were made of 16 AWG tinned copper wire (Belden, 8013) and were incorporated into an electrical design with active and passive detuning mounted over different tuning capacitors (Figure 3A). A variable tuning capacitor was used for initial adjustments then replaced with a fixed component to increase coil reliability. To increase coil safety, all loops were provided with fast non-magnetic fuses (Siemens Healthineers, Erlangen, Germany) with a rating of 315 mA at the operating frequency. A 65-mm-long semirigid coaxial cable (Carlisle, UT-85C\_FORM) allowed for separating all preamplifiers from the loops to minimize the noise figure, increase stability, and reduce the interaction with Tx elements. Cable traps were integrated into the output cables to reduce undesirable crosstalk between receive channels and coupling with the Tx-coil. The selected preamplifiers (Siemens, 10185 702 E2) also had internal cable traps between the first and second amplification stage.

After assembling the receive coil and adjusting all active and passive detuning circuits, the output impedance of the Rx loops was set as close as possible to  $75 \Omega$  to optimize the noise matching of the selected preamplifiers. Coupling was subsequently evaluated by measuring the transmission coefficient between all possible loop combinations for both the posterior and the anterior subarrays. For this purpose, 75-to- $50 \Omega$  transformers were inserted between the input connectors of the preamplifier socket boards and the vector network analyzer (VNA) probes. All nontested elements were detuned. The Tx coil was not installed during these tests to facilitate access to the socket boards, as this was found to cause negligible effects on the Rx coil parameters.

### 2.1.2 | Transmit coil

The transmit design was based on full-wave electromagnetic simulations performed in CST Studio Suite. Eight dipoles of two different lengths were selected as transmit elements. Each dipole was modeled as having three ports: two ports representing tuning inductors and one central port representing a parallel matching capacitor. Tuning and matching were accomplished by means of a co-circuit simulation.

The  $B_1^+$  distribution within the phantom was simulated for comparison with experimental results and subsequent validation of the coil model. Simulated  $B_1^+$  maps of individual transmit elements were scaled to equate the mean phase and 95th percentile of their magnitude to experimental  $B_1^+$  maps, as described in an earlier work,<sup>56</sup> ensuring agreement between simulated and experimental maps. The simulated and experimental  $B_1^+$  maps of individual transmitters were combined in circularly polarized (CP) mode and with 10,000 different random RF shim settings: the difference between the predicted combined  $B_1^+$  maps (mean and 95th percentile) was calculated to quantify their agreement over a large range of shim solutions.

With the coil model validated through phantom simulations, four CST body models were simulated (Hugo, Gustav, Laura, and Donna) for use in online SAR monitoring. Local SAR matrices (Q-matrices) were derived for each body model and catenated prior to compression into virtual observation points (VOPs)<sup>57</sup>: the catenation of multiple body models of varying size and position ensured that the worst case scenario for local SAR would be implemented on the scanner. To account for additional inaccuracies in coil modeling, differences in the population and inaccuracies in the online measurement,<sup>58</sup> a conservative safety factor of 2.0 was added to the SAR prediction.

To construct the transmit coil, the dipoles were machined from copper-clad Garolite. All dipoles were 1.6-cm wide with rounded ends to mitigate high conservative electric fields. Figure 2B shows the structure of the posterior Tx elements. Anterior and posterior elements were 38.1-cm

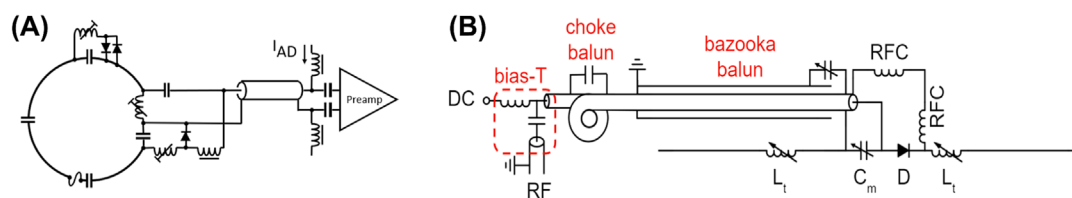


**FIGURE 3** Electrical schematic of the (A) Rx and (B) Tx elements.

long to provide adequate coverage from the occipital pole to the fourth thoracic vertebrae. Alternatively, the length of the lateral dipoles was set at 22.1 cm in practice to avoid the impediment of the subject's shoulders; however, a commensurate benefit to offsetting their  $B_1^+$  profiles with respect to the longer dipoles was an enhanced ability to RF shim over the longitudinally oriented spinal cord. The distance between dipoles (a minimum of 10 cm) was chosen to permit a level of coupling that could be compensated for with RF shimming. The distance between any dipole and the center of the imaging region (C3) ranged from approximately 14 to 22 cm; this distance was a compromise between transmit uniformity and efficiency. The sparse geometry of transmit dipoles (Figure 2D) was also selected to allow receive-coil preamplifiers to be placed in regions that would reduce interaction between the constituent coils. Thus, the lateral transmit elements were placed 5 cm from the nearest preamplifier to mitigate coupling and the corresponding adverse effects to coil performance.

Two high-Q inductors (approximately 10–80 nH, depending on dipole length and load) were incorporated into each dipole to electrically shorten them to resonate at 297.2 MHz. The electrical design is presented in Figure 3B. Dielectric coupling between the ends of the posterior (long) dipoles and the supports caused their resonant frequency to shift by approximately 55 MHz; therefore, the housing beneath Tx-8 and the polycarbonate supports beneath Tx-3 to 5 were hollowed out to decrease the frequency shift and allow for these elements to be tuned to the correct frequency. Although this was also done for the shorter dipoles for mechanical reasons, it was not necessary as they required a larger tuning inductance.

An electrically shortened bazooka balun (Belden 9222 triaxial cable, Johanson 59H01 high-power variable capacitor) and a hand-made cable trap (distal to the bazooka balun and dipole input) were installed between each dipole and its transmission line to attenuate common-mode RF currents. A parallel matching capacitor (Johanson 59H01, 1–25 pF, rated to 1000 V<sub>DC</sub>) was employed to match dipoles to 50 Ω. Active detuning was achieved with a serial high-power PIN diode (Chelton DH80106-44 N) that was forward biased through RF chokes (CoilCraft 1812CS-102XJEB, 1 μH, self-resonant frequency: 310 MHz) during transmission.

The Tx dipoles were installed and tuned with the Rx array already adjusted. The coil was placed inside a mock RF shield and loaded with the phantom to measure the Tx S-parameters with the Rx array detuned. This measurement was repeated with two volunteers. The S-parameters were later compared with the matrix obtained from the scanner RF safety watchdog log. Coupling to the Rx coil in the receive mode was also measured on the bench.

### 2.1.3 | Phantom

For this study, we designed a 45-cm-tall head-neck phantom, with a 31-cm-wide section of the upper thorax (Figure 1C), by using the 3D average head model as a reference. The resulting head circumference was 60 cm, which is in the large range for an average adult male. Its inner volume was exported to CST to be used as the coil load during simulations. The phantom housing was 3D-printed in PLA (EcoTough PLA 2.0), waterproofed with an interior coating of epoxy (Smooth-On XTC-3D High Performance Coating), and externally reinforced with the same epoxy and fiberglass (120–38 Standard E-Glass fiberglass cloth). It was filled with a solution based on a published recipe.<sup>59</sup> The phantom contained the following ingredients per liter: demineralized water (398 ml), sugar (778 g), salt (106 g), alcohol-free mouthwash (40 ml), and Gadovist 1.0 (1 ml). A conductivity of 0.6 S/m and a relative permittivity of 35.5 were measured at 300 MHz with an Agilent 85070E dielectric probe. These parameters mimic the estimated average of the biological tissues that constitute the region to which the coil is sensitive. This was verified on the bench by comparing reflection coefficients measured on different Rx loops loaded with the phantom and three volunteers. Finally, the phantom was used as a load during the bench and scanner tests. The CAD model and recipe for the phantom fabrication is available at: <https://github.com/neuropoly/phantom-spinoza> (we used v5 for this paper).

## 2.2 | Coil evaluation in the MRI room

### 2.2.1 | Safety

The ethics committees of the scanning sites approved all in vivo 7-T MRI studies presented in this work. Examinations were performed on 15 adult healthy volunteers who gave written informed consent.

MRI tests were performed in a MAGNETOM Terra scanner (Siemens Healthineers, Erlangen, Germany), using the parallel transmission (pTx) research mode. The integrity of coil components during high peak-power, high-SAR, and high gradient-strength pulse sequences is critical to ensure the safe operation of the coil during routine use.<sup>60</sup> Coil heating was evaluated prior to and subsequent to a SAR-intensive sequence (operating at approximately twice the permissible SAR level for human scanning in first-level controlled mode<sup>61</sup>) with an infrared camera. Commensurate temperature evaluation was conducted for high peak-power and gradient-intensive scans. No discernible increases in housing temperature were measured; therefore, the coil user is limited only by patient SAR (as described below) and not by the power-handling capacity of the coil.

## 2.2.2 | Receive coil sensitivity profile

The sensitivity profile of individual receive coil elements was reconstructed from a sagittally oriented fast low-angle shot (FLASH) scan (in-plane FOV = 320 × 302 mm<sup>2</sup>, matrix size = 192 × 144, number of slices = 5, slice thickness = 5 mm, slice gap = 15 mm, TR/TE = 8/3.69 ms, flip angle [FA] = 20°, and BW = 320 Hz/pixel).

## 2.2.3 | SNR and geometry factor

SNR and geometry factor (g-factor) maps were acquired using a gradient echo (GRE) scan. A sagittal scan with in-plane FOV = 384 × 384 mm<sup>2</sup>, matrix size = 256 × 256, number of slices = 13, slice thickness = 2 mm, slice gap = 0.4 mm, TR/TE = 30/6 ms, FA = 12°, averages = 2, and phase-encoding direction = superior–inferior, was acquired to map the g-factor along the superior–inferior and right–left directions. An axial scan was acquired to map the axial g-factor, with in-plane FOV = 192 × 192 mm<sup>2</sup>, matrix size = 384 × 384, number of slices = 7, slice thickness = 5 mm, slice gap = 5 mm, TR/TE = 30/6 ms, FA = 12°, averages = 2, and phase-encoding direction = right–left.

The scans were repeated without RF excitation to derive the noise covariance matrix. SNR maps were calculated using the root-sum-of-squares approach,<sup>9,62</sup> while g-factor maps were derived from the coil sensitivities and noise correlation information.<sup>21</sup> B<sub>1</sub><sup>+</sup> field effects on SNR were removed by dividing the SNR maps by the sine of the measured FA.

## 2.2.4 | B<sub>1</sub><sup>+</sup> mapping and RF shimming

In vivo B<sub>1</sub><sup>+</sup> maps of individual transmit elements were acquired with a vendor-provided presaturation turbo-FLASH pulse sequence<sup>63</sup> with the following parameters: FOV = 388 × 240 mm<sup>2</sup>, matrix size = 196 × 120 mm<sup>2</sup>, sagittal orientation, number of slices = 28, slice thickness = 3.2 mm, TR/TE = 6970/1.79 ms, saturation FA = 90°, excitation FA = 10°, and BW = 550 Hz/pixel. These maps were combined offline using three different shim settings: (i) the nominal CP mode (i.e., a phase-only shim that produced the highest efficiency in C3); (ii) maximizing B<sub>1</sub><sup>+</sup> uniformity by minimizing the standard deviation over the mean B<sub>1</sub><sup>+</sup> along the spinal cord between the upper thorax and the occipital region; and (iii) maximizing the B<sub>1</sub><sup>+</sup> efficiency over the same region. Subsequently, the SAR efficiency of the B<sub>1</sub><sup>+</sup> field was calculated using the maximum 10-g-averaged SAR derived from the local SAR matrices (excluding the 2-fold safety factor utilized for human scanning). All B<sub>1</sub><sup>+</sup> shimming calculations were performed in MATLAB.

A Magnetization Prepared 2 Rapid Acquisition Gradient Echo (MP2RAGE)<sup>64</sup> scan was acquired in CP mode and sagittal orientation, FOV = 256 × 224 × 192 mm<sup>3</sup>, 1 mm<sup>3</sup> isotropic resolution, TR/TE = 3250/1.83 ms, TI1/TI2 = 840/2370 ms, FA1/FA2 = 5/6°, in-plane acceleration factor = 3, and BW = 250 Hz/pixel.

The spinal cord between C1 and T5 was segmented from the GRE image of the second inversion time (INV2) of the MP2RAGE scan using Spinal Cord Toolbox<sup>65</sup> and was used as a mask for B<sub>1</sub><sup>+</sup> shimming, as described below.

Using Shimming Toolbox,<sup>66</sup> a set of eight complex shim weights (**w**) was calculated offline, such that the resulting B<sub>1</sub><sup>+</sup> efficiency would be uniform across the spinal cord:

$$F(\mathbf{w}) = \sum^{N_{\text{voxels}}} (|B_1^+ \mathbf{w}| - t)^2,$$

where  $F(\mathbf{w})$  is the cost function to be minimized via B<sub>1</sub><sup>+</sup> shimming,  $t$  is the target B<sub>1</sub><sup>+</sup> efficiency of 15 nT/V, B<sub>1</sub><sup>+</sup> is the B<sub>1</sub><sup>+</sup> map for all Tx channels, and B<sub>1</sub><sup>+</sup>**w** is the B<sub>1</sub><sup>+</sup> map for all Tx channels after the shim weights, **w**, are applied. Shim-weight optimization was performed using the *Shimming Toolbox*. During the optimization process, local SAR was constrained and set to not exceed the maximum local SAR obtained with the CP mode by more than 50%; local SAR was computed using VOPs.<sup>57</sup>

Using the shim weights, **w**, B<sub>1</sub><sup>+</sup> maps and a new MP2RAGE scan were re-acquired and masked using the spinal cord mask described above. Signal intensity, T1 value, and B<sub>1</sub><sup>+</sup> efficiency within this mask were analyzed for the MP2RAGE INV2 images, MP2RAGE T1 maps, and in vivo B<sub>1</sub><sup>+</sup> maps, respectively, along with the coefficient of variation (CoV).

## 2.2.5 | Comparison with other coils

An identical coil was built and supplied to a second site (MGH Martinos Center for Biomedical Imaging, USA) to perform multicenter studies. This coil version was compared with two different coils<sup>67</sup>: an eight-Tx/32-Rx brain coil (Nova Medical, Wilmington, MA, USA) and a custom-built



16-Tx/64-Rx head-neck coil.<sup>5</sup> SNR quantitative maps were calculated by means of a root-sum-of-squares reconstruction with noise-covariance weighting of the individual channel data.<sup>9,62</sup> A GRE sequence was used (TR = 8000 ms, TE = 3.82 ms, FOV = 256 mm, voxel size =  $1 \times 1 \times 2 \text{ mm}^3$ , number of slices = 130, FA = 78°, bandwidth = 340 Hz/px, reference amplitude = 500 and 0 V). For each coil, the optimal SNR combination was then divided by the sine of the FA to remove variations due to transmit-field nonuniformities.<sup>68</sup> A ROI was manually drawn on the acquired images to calculate the SNR profiles along the z-axis from the spine to the brain.

### 3 | RESULTS

#### 3.1 | Receive coil

With the Rx coil completely adjusted and loaded with the phantom, the mean output impedance measured at the input sockets of the preamplifiers, towards the loops, was  $75.3 \pm 3.9 \Omega$ ; the reactance, which was reduced to a minimum during the adjustments, showed a mean of  $-0.6 \pm 0.3 \Omega$ . A confidence level of 95% was used here and in all the following data. Coupling ( $S_{nm}$ ) measured under the same loading conditions showed close agreement with values predicted by simulation. Table 1 shows the mean coupling values between adjacent loops and the overall coupling obtained separately from each subarray without including the effect of preamplifier decoupling. The simulated average coupling between both subarrays was  $-32.4 \pm 2.4 \text{ dB}$ ; only simulations were used in this case because measurements on the independent sections showed that the CST model of the coil was accurate. As expected, the highest coupling ( $\approx -7 \text{ dB}$ ) was obtained, and later verified by measurements, from the pairs of loops 8–17 and 12–16. These are the elements from different subarrays that are positioned at the closest distance, without being critically overlapped (Figure 2C). The mean value of measured preamplifier decoupling was  $-18.3 \pm 2.6 \text{ dB}$ .

Images acquired with the individual channels, shown in Figure 4, demonstrated the coverage over the ROI and limited coupling between Rx elements. Figure 5 shows in vivo SNR maps over the central sagittal plane and an axial plane located at the C3-C4 segment. The SNR along the spinal cord increases from the thoracic to the occipital region, which is in agreement with the increase in density and proximity of receive elements. Figure 6 shows the inverse g-factor (1/g) maps, where typical values for one-dimensional (1D) and two-dimensional (2D) accelerations were obtained from slices that will be regularly selected during spinal cord studies. Noise enhancement in the spinal cord is in an acceptable range up to a 1D acceleration factor of 4. As for 2D acceleration, less desirable noise amplification values start to appear from  $R = 3 \times 3$ .

#### 3.2 | Transmit coil

The mean impedance of bazooka baluns and RF chokes was 710 and 1130  $\Omega$ , respectively. No sensitivity to touching or repositioning of the transmit cable was observed, which demonstrated that the combination of a bazooka balun and RF choke was sufficient to achieve common mode suppression.

The maximum and mean coupling between adjacent transmit elements, when measured on the bench, inside the mock RF shield, with the coil loaded by the phantom and the Rx-coil detuned, were  $-7.7$  and  $-16.5 \pm 6.5 \text{ dB}$ , respectively. The mean coupling between all elements was  $-23.4 \pm 2.8 \text{ dB}$ . The mean reflection was  $-32.6 \pm 2.3 \text{ dB}$ . The corresponding S-parameter matrix is shown in Figure 7A. A similar matrix was obtained from the scanner with the same phantom (Figure 7B). In this case, the maximum and mean coupling between adjacent transmit elements were  $-7.9$  and  $-15.6 \pm 6.3 \text{ dB}$ , respectively. The mean coupling between all elements was  $-23.8 \pm 3.5 \text{ dB}$ . The mean reflection was  $-23.5 \pm 2.3 \text{ dB}$ . The adequate similarity observed between the two matrices validated the adjustments performed on the bench. Active detuning provided a mean isolation of  $-21.5 \pm 2.3 \text{ dB}$  with the receive coil during reception.

Simulated  $B_1^+$  efficiency and  $B_1^+ / \sqrt{\max(\text{SAR}_{\text{local}})}$  are shown in Figure 8 for the four CST body models incorporated into the VOPs. The maximum 10-g-averaged SAR is located in the nose for a large human model, like Hugo, due to the close proximity of the anterior dipole. For small-to-average size human models, the maximum local SAR occurs in the neck region.

**TABLE 1** Mean coupling values showing good agreement between bench measurements and initial simulations.

Mean coupling, $S_{nm}$ , in dB	15-Ch (posterior)		5-Ch (anterior)	
	Measured	Simulated	Measured	Simulated
Adjacent	$-15.6 \pm 0.9$	$-15.8 \pm 2.4$	$-16.3 \pm 1.3$	$-17.2 \pm 1.9$
Overall	$-22.3 \pm 1.7$	$-23.6 \pm 2.1$	$-16.6 \pm 1.2$	$-17.3 \pm 1.4$

Note: In both cases, the phantom was used to load the coil. These coupling values were a reasonable starting point for the subsequent implementation of preamplifier decoupling.

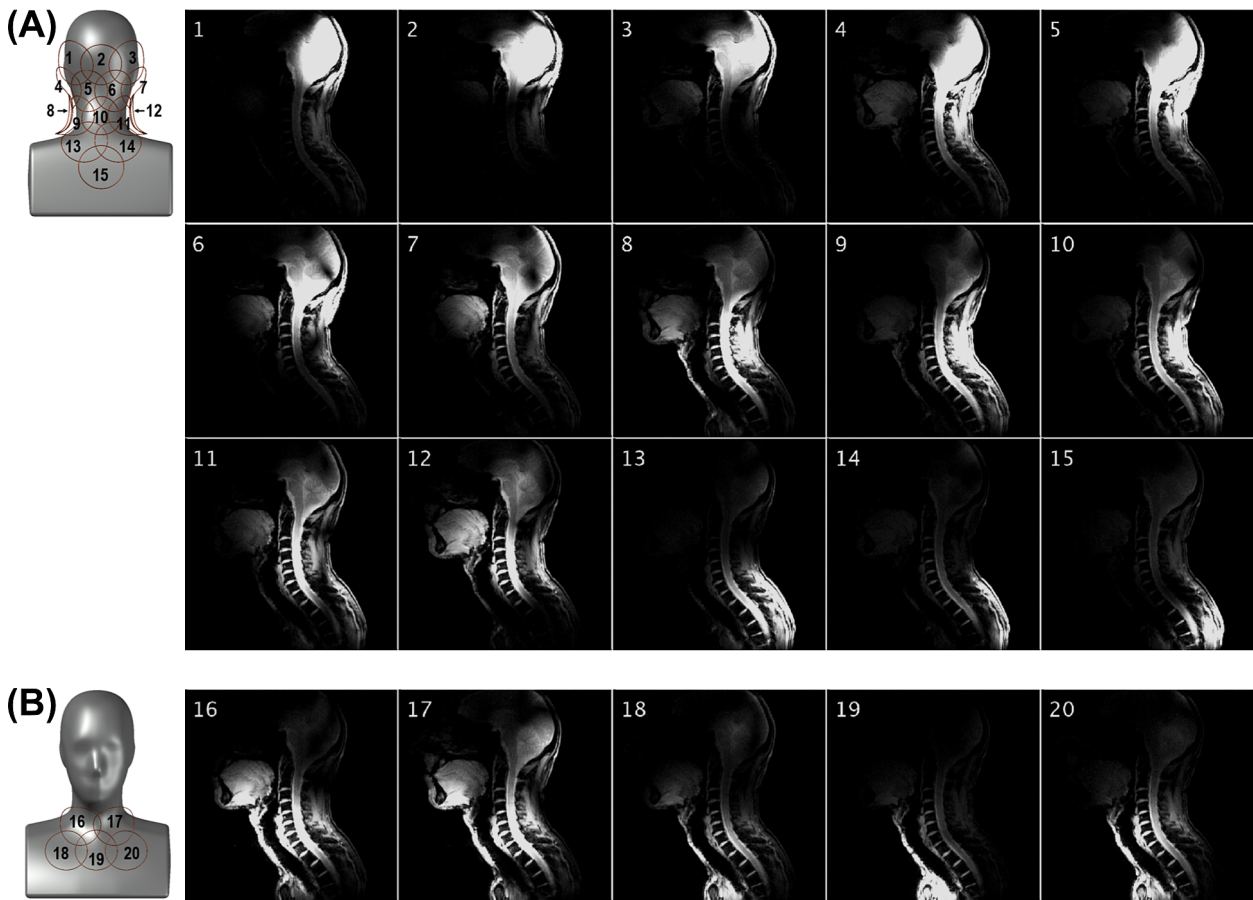


**FIGURE 4** Sensitivity profile of the (A) Posterior and (B) Anterior Rx subarrays obtained with a FLASH sequence with a FOV of  $320 \times 320$  mm and a  $512 \times 512$  matrix. The intensity colormap scaling was kept the same across the 20 panels. FLASH, fast low-angle shot; FOV, field of view.

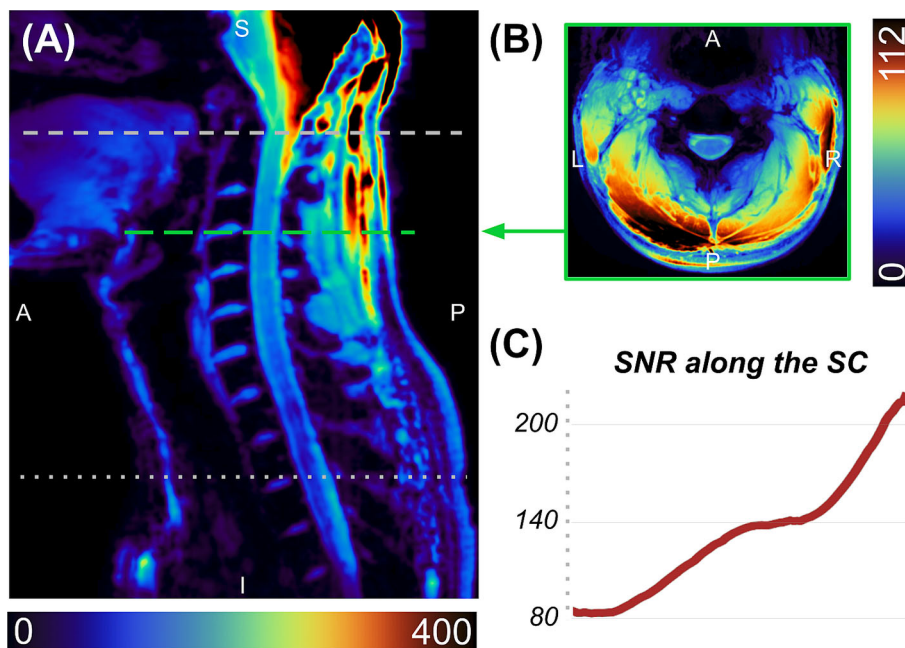


**FIGURE 5** Signal-to-noise ratio (SNR) maps along (A) The sagittal midline and (B) The C3-C4 level. (C) SNR along the spinal cord (SC) ranges from 80 at the T2-T3 disc to 200 at the top of the C1 vertebra.

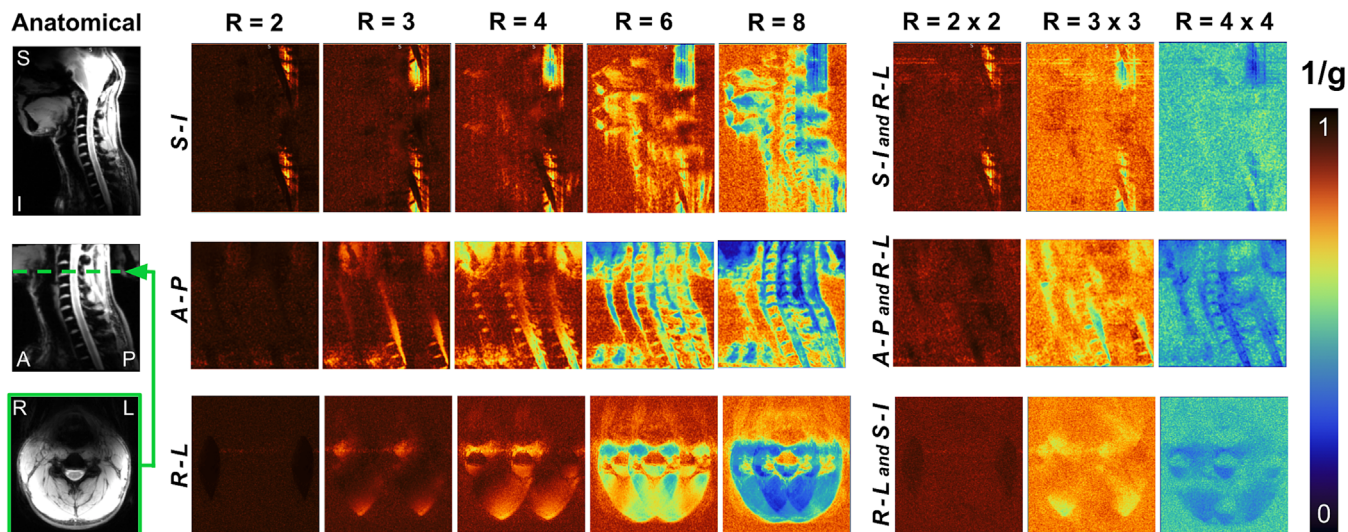


**FIGURE 6** Maps of the inverse g-factor ( $1/g$ ) showing (top) the sagittal midline with acceleration in the superior–inferior and right–left directions, (middle) the sagittal midline with acceleration in the anterior–posterior and right–left directions, and (bottom) axially, at the C3–C4 level, acceleration factors in the right–left and superior–inferior directions. g-factor, geometry factor.

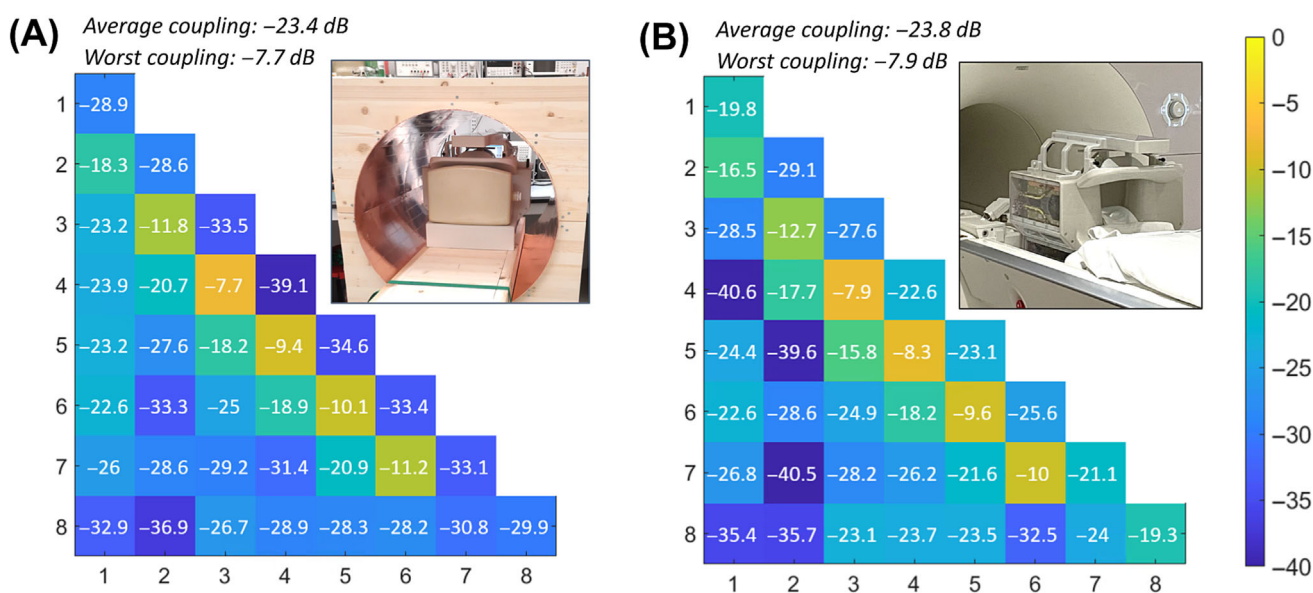


**FIGURE 7** S-parameter matrices of the Tx coil measured (A) On the bench inside a mock radiofrequency shield, and (B) Obtained from a scanner, showing a fair resemblance.

### 3.3 | $B_1^+$ shimming

RF shimming capabilities of the coil were demonstrated by simulations performed on the validated coil model (see the [supporting information](#)). Implementation examples are shown in Figure 9. In all cases, the spinal cord was segmented using the Spinal Cord Toolbox and overlapped on the original images. A comparison of two  $B_1^+$  efficiency combinations generated from individually acquired  $B_1^+$  maps is shown in Figure 9A, in CP mode (left) and with optimized shim weights (center). Figure 9B shows the signal intensity of GRE images from the second inversion time, while Figure 9C shows the estimated T1 values. The shim weights were optimized to minimize the CoV along the spinal cord. The profiles corresponding to the segmented spinal cords are shown in the right panels for ease of comparison.

CP mode excitation resulted in an inhomogeneous excitation profile, with high  $B_1^+$  efficiency and corresponding high signal intensity at the upper cervical levels, with a steep drop from  $\sim$ C4 to  $\sim$ T2, as shown in the left and right panels of Figure 9A,B. RF shimming resulted in a more

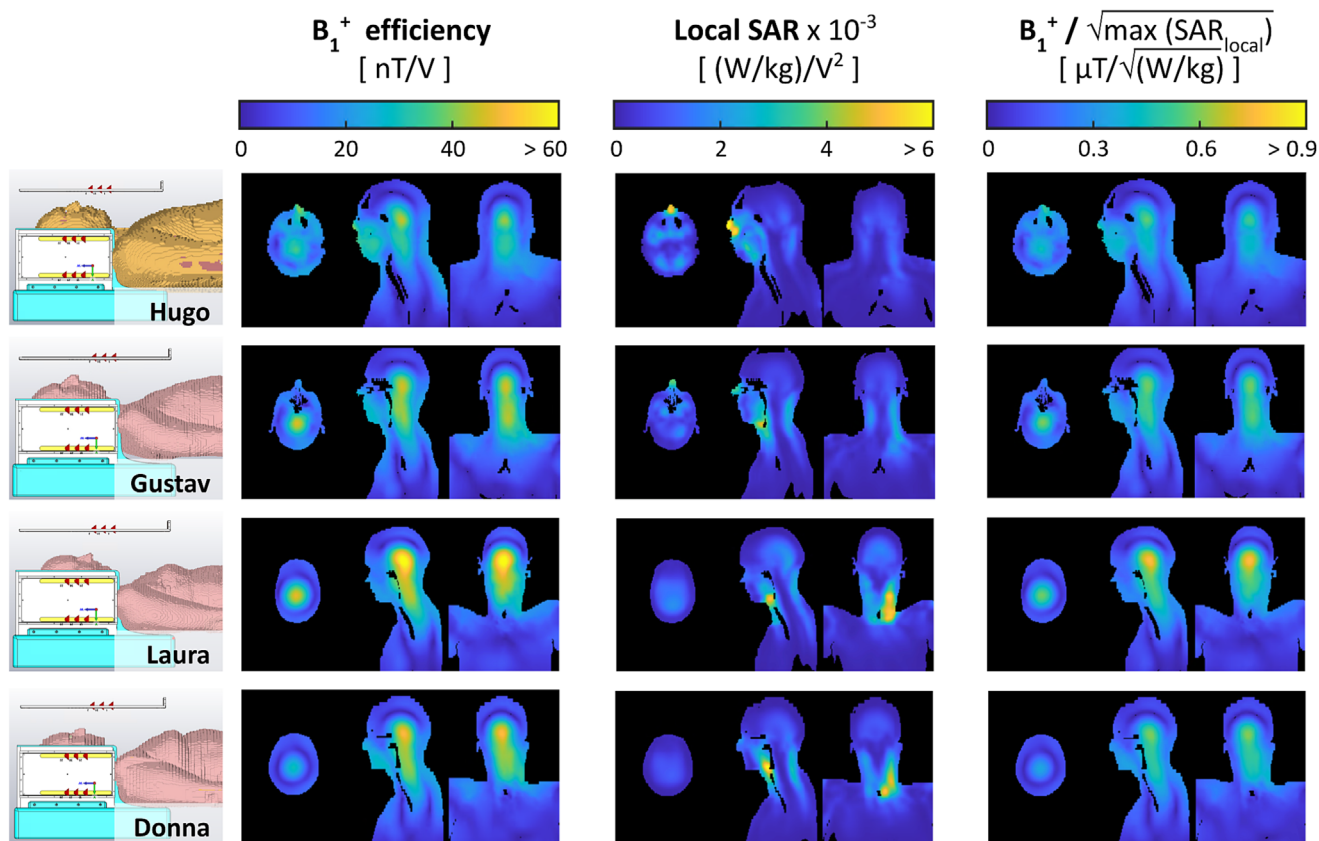


**FIGURE 8** Simulated  $B_1^+$  efficiency, 10-g-averaged SAR efficiency, and  $B_1^+$  efficiency per square root of the maximum local SAR for four CST body models (shown on the left: Hugo, Gustav, Laura, and Donna) when driven in the nominal CP mode. The maximum local SAR occurs in the nose for a large body model like Hugo (due to close proximity with the anterior transmit dipole), and in the neck for small-to-average-sized body models. All four body models were incorporated into online SAR matrices, the diversity of which ensured a conservative estimate of local SAR. CP, circularly polarized; SAR, specific absorption rate.

homogeneous excitation profile, as evidenced by a reduction of CoV by  $\sim 76\%$  (from 0.263 to 0.062) for  $B_1^+$  efficiency and 23% (0.411 to 0.316) for GRE signal intensity. The measured  $B_1^+$  efficiency for RF shimming (14.44 nT/V) is in line with the targeted  $B_1^+$  efficiency of 15 nT/V.

Improved  $B_1^+$  homogeneity resulted in more uniformity along the spinal cord for estimated T1 values, as evidenced by a CoV reduction of  $\sim 35\%$  (0.135 to 0.087). Additionally, while the T1 values estimated in the CP mode show a marked reduction in the upper cervical levels (and a similar increase in the upper thoracic spine), T1 values estimated from the RF shimmed MP2RAGE scan are relatively uniform along the FOV.

### 3.4 | Comparison with other coils

Figure 10 shows an SNR comparison of the proposed coil and the two available alternatives.<sup>67</sup> The SNR map revealed adequate uniformity (CoV = 10.2%) from the occipital lobe to the midthoracic spine, while showing a 30.4% increase in mean SNR ( $\text{SNR}_{\text{head/neck}} = 246.9$ ,  $\text{SNR}_{\text{head}} = 90.9$ ,  $\text{SNR}_{\text{spine}} = 321.9$ ) with respect to the head-neck, which was designed to include the spine region as well. The SNR declines in the upper part of the studied region, which comprises most of the brain, but useful values were registered in the occipital region.

## 4 | DISCUSSION

The development of MRI coils to study a region extending from the occipital lobe to the T4-T5 vertebral level at 7 T has to overcome several challenges to generate a uniform excitation field and achieve high sensitivity. Most of these challenges are caused by the length, curvature, and location of the spinal cord itself, and the complex anatomy of this region, characterized by a variety of tissues, dimensions, and morphological differences within the population. In this work, we present an eight-channel transmit and 20-channel receive coil that addresses these challenges. Testing of this coil showed excellent performance over an extended range beyond the cervical spine, including the occipital and upper thoracic

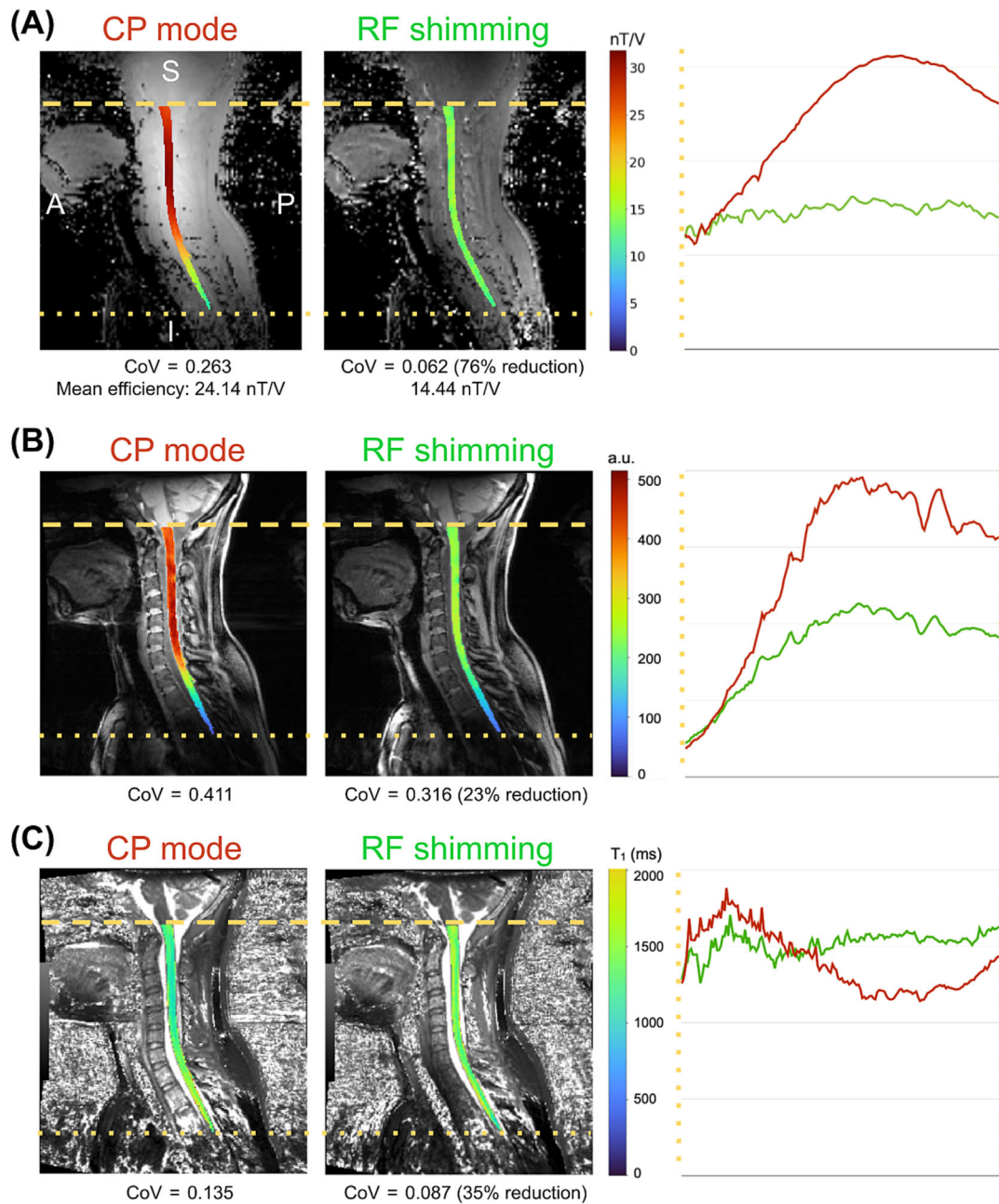


**FIGURE 9** Example of the effect of RF shimming for optimal uniformity on (A) The  $B_1^+$  map, (B) The GRE scan, and (C) T1 maps from the MP2RAGE sequence. CoV, coefficient of variation; GRE, gradient echo; MP2RAGE, Magnetization Prepared 2 Rapid Acquisition Gradient Echo; RF, radiofrequency.

regions, when compared with other coils.<sup>5,6</sup> The Tx and Rx coils are integrated into a single housing equipped with hinges that allow it to be easily opened and closed to expedite the placement of the subject. In addition, the position of the anterior portion of the receive coil can be adjusted to better conform to the anatomy of the subject.

#### 4.1 | Rx coil

The difficulties involved in conceiving a receive array adapted to this complex anatomical region and the need to know the exact geometry of the receive coil for future experiments motivated the use of CST simulations to carry out the design task. The time spent on the simulations was compensated for by the resulting simplified assembly and adjustment, especially of the critical overlap between adjacent elements, which is also a

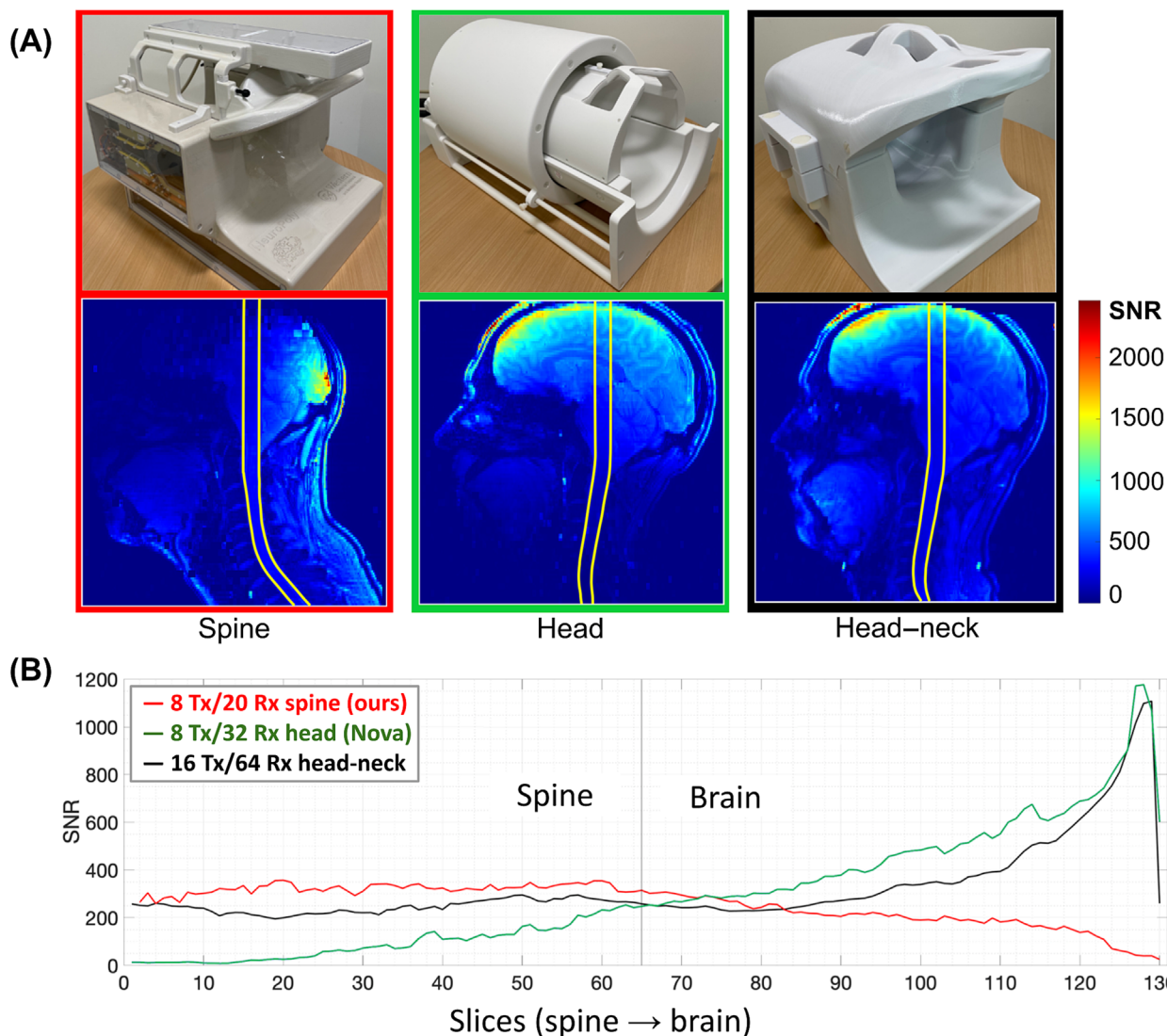


**FIGURE 10** Signal-to-noise ratio (SNR) assessment and comparison with two different coils displaying (A) SNR maps and (B) Profiles. Each point on the profiles is the average SNR within the region of interest shown on the corresponding maps for each slice.<sup>67</sup>

time-consuming task. In this regard, it was not necessary to empirically reshape the wire loops once they were mounted directly into the grooves created on the coil formers, because the inductive decoupling values achieved in the simulations were preserved.

Considering that the coil design also includes preamplifier decoupling, the mean adjacent coupling achieved (−16 dB) was in the range of acceptable limits.<sup>69</sup> In some cases (loops 5–6, 9–10, 6–12, and 16–17), the best possible  $S_{nm}$  values were between −10.6 and −12 dB, mainly because of loop shapes that favored coupling. The worst overall values (−7.1 dB), obtained for loop pairs 8–17 and 12–16, were caused by the proximity of the respective elements when the anterior (adjustable) array section was placed at its closest position to the fixed posterior, to better adapt the array to the phantom; however, these values improved when the array was adjusted for a larger load, because elements 16 and 17 are moved away from 12 and 8, respectively. In all cases, the proximity between the simulated and measured coupling values confirmed the validity of the simulations.

Comparison with other coils (head and head-neck) with more channels demonstrated that 20 receive loops, with convenient dimensions and placement, were sufficient to obtain higher SNR along the spinal cord.<sup>5</sup> The improvement compared with the head-neck coil—the available coil that also targets the neck region—was mainly due to the greater distance from the Rx elements to the subject and the larger loop size of the head-neck coil in the neck region. This coil was designed with a fixed structure to accommodate almost all human subjects, resulting in additional space for most individuals, which affects the SNR at 7 T. Conversely, the position of the anterior five elements of the neck coil can be adjusted to be in close proximity to the anterior region of the subject's neck, increasing coil sensitivity in the C-spine. Average g-factors obtained during the same study over an axial plane positioned at level C3 of the cervical spine showed similar values for all coils up to acceleration factors (R) of 4, while reductions of 27% (0.67/0.49) and 22% (0.63/0.49), respectively, were observed for R = 6. This is an expected result, mainly due to the

lower number of Rx channels of the proposed coil. Even although one of the initial objectives was to build a coil with a minimum number of channels, both aspects could benefit slightly from the addition of a Rx element near the upper thorax without significantly increasing the complexity of the coil.

## 4.2 | Tx coil

The cervical spinal cord is located considerably deep into the body and has a characteristic curvature that causes a variable distance to the elements of any coil along the Z-axis. This combination presents a difficulty in attaining high power efficiency and entails the use of RF shimming to produce a homogeneous excitation field at 7 T. The presence of the shoulders adds disparate geometrical constraints along Z. They prevent the use of a volume coil that surrounds the spinal cord closely enough to operate with acceptable efficiency and with sufficient length to cover our desired ROI (down to the upper thorax).

Dipoles were selected for the Tx coil primarily for the ability of their geometrical properties to address the specific challenges described above. The physical length of loaded, half-wavelength dipoles at 7 T (approximately 44 cm when near the head<sup>46</sup>) allowed for a transmit coil to be developed with an extended  $B_1^+$  coverage along the superior–inferior axis, despite being limited to only eight transmit channels (a ubiquitous specification for ultrahigh field scanners at present). The holistic approach in designing the receive array resulted in high decoupling between both coils. This was highly influenced by the selection of nonuniform spacing between transmit dipoles, which created sufficient clearance to place the preamplifiers and other receive components. As a result, the tuning process of both coils was significantly simplified, as it was possible to perform them independently. In this way, we avoided the difficulties inherent to Tx/Rx coils with highly coupled and closely spaced arrays, as encountered in the early stages of other works,<sup>3,5</sup> while protecting the Rx coil during the Tx mode and potentially reducing local SAR.

With each individual element being sensitive to a larger region of the body, a volume-like multichannel topology could be implemented, while still maintaining close proximity to the ROI. The resultant higher field intensities in the central region (i.e., central brightening), characteristic of volume coils, increased the efficiency around the spine. Volume coils, in comparison with planar coil arrays, are compatible with automatic and convergent transmit-power calibration when scanning: a significant advantage for clinical workflows. The multichannel design could then be used for RF shimming to further improve the performance of the coil over an extended FOV.

RF shimming over the longitudinally oriented spinal cord was further benefited by the difference and offset of the  $B_1^+$  profiles of the lateral dipoles with respect to those located in the posterior and anterior sections of the coil. Therefore, the FOV along the superior–inferior axis was lengthened, which made it possible to study an elongated ROI extending from the occipital lobe to T4–T5 vertebral levels. The results obtained in this region showed higher power efficiency and lower SAR than other solutions where pTx was not implemented.<sup>6</sup> In addition, RF shimming can provide a range of solutions, depending upon the application. Simulations showed that the coil offered the flexibility required to implement  $B_1^+$  shimming solutions in this region to improve transmission uniformity, efficiency, or SAR according to the requirements of the pulse sequence. Trade-offs between these parameters can also be obtained by modifying the regularization of the cost functions.

The improvements offered by the Rx and Tx characteristics of the coil offer many potential clinical applications. The increased coverage in the inferior–superior direction enables the detection of lesions and pathologies up to the upper thoracic levels (T4–T5), allowing, for example, a more complete characterization of the lesion load in multiple sclerosis. Good imaging performance up to an acceleration factor of 4 may be used to shorten the scan time and reduce patient discomfort, while the increased SNR may be used to increase resolution and thereby enable the detection of smaller pathologies compared with current clinical practice. The pTx capabilities of the coil may be used to improve  $B_1^+$  homogeneity on a per-patient basis via RF shimming, as demonstrated in this paper, to enable the development of universal pulses for the cervical and upper thoracic spinal cord.<sup>70,71</sup> While the coil was designed to fit a wide range of anatomical shapes, some clinical populations, such as those with an extremely high body mass index, might be unable to be accommodated.

In conclusion, this work presents a transmit/receive coil, composed of eight pTx dipoles and 20 anatomically shaped semiadaptable Rx loops, for spinal cord imaging at 7 T. The coil was designed, tested, and validated by simulations, on the bench and in the scanner. RF shimming allowed optimization of  $B_1^+$  uniformity,  $B_1^+$  efficiency, or SAR efficiency. An extended FOV covering from the occipital lobe to the upper thoracic spine was demonstrated with several volunteers. A comparison with available coils revealed improved performance parameters in the spinal cord region. This coil solution therefore provides a convincing platform for producing the high image quality necessary for clinical and research scanning of the upper spinal cord.

## ACKNOWLEDGMENTS

The authors thank Justin De Meulemeester for helping with VOP creation, Dr. Pedram Yazdanbakhsh and the 7 T team at the Brain Imaging Center of the Montreal Neurological Institute for technical support during imaging, and Dr. Marcus Couch, Dr. Omer Oran, and Dr. Yulin Chang from Siemens Medical Solutions for technical support. JCA received financial support from the Canada Research Chair in Quantitative Magnetic Resonance Imaging (CRC-2020-00179), the Canadian Institute of Health Research (CIHR FDN-143263), the Canada Foundation for Innovation (32454, 34824), the Fonds de Recherche du Québec - Santé (322736), the Natural Sciences and Engineering Research Council of Canada

(RGPIN-2019-07244), the Canada First Research Excellence Fund (IVADO and TransMedTech), the Quebec Biolmaging Network (5886, 35450), and Mila - Tech Transfer Funding Program. KMG received financial support from the Canada Foundation for Innovation, Canada First Research Excellence Fund to BrainsCAN, and Brain Canada Platform Support Grant. Imaging performed at the Athinoula A. Martinos Center for Biomedical Imaging used funds from Biotechnology Resource Grants provided by the National Institute of Biomedical Imaging and Bioengineering of the National Institutes of Health (NIH) to the Center for Functional Neuroimaging Technologies (P41EB015896), the Center for Mesoscale Mapping (P41EB030006), and RLB (R01EB027779). Also, LLW received support from the Office of the Director of the NIH (S10OD023637). The content is solely the responsibility of the authors and does not necessarily represent the official views of the NIH.

## CONFLICT OF INTEREST STATEMENT

The authors declare no potential conflict of interest.

## ORCID

Nibardo Lopez-Rios  <https://orcid.org/0000-0002-4791-8260>

Daniel Papp  <https://orcid.org/0000-0003-1481-1413>

## REFERENCES

- Barry RL, Johanna Vannesjo S, By S, Gore JC, Smith SA. Spinal cord MRI at 7T. *Neuroimage*. 2018;168:437-451.
- Zhao W, Cohen-Adad J, Polimeni JR, et al. Nineteen-channel receive array and four-channel transmit array coil for cervical spinal cord imaging at 7T. *Magn Reson Med*. 2014;72(1):291-300.
- May MW, Hansen SLJD, Kutscha N, et al. A patient-friendly 16ch Tx / 64ch Rx array for combined head and neck imaging at 7 Tesla. In: ISMRM 2021; 2021. <https://submissions2.miramsmart.com/ISMRM2021/ViewSubmission.aspx?sblID=363&validate=false>
- Pfaffenrot V, Brunheim S, Rietsch SHG, et al. An 8/15-channel Tx/Rx head neck RF coil combination with region-specific B1 + shimming for whole-brain MRI focused on the cerebellum at 7T. *Magn Reson Med*. 2018;80(3):1252-1265.
- May MW, Hansen SLJD, Mahmutovic M, et al. A patient-friendly 16-channel transmit/64-channel receive coil array for combined head-neck MRI at 7 Tesla. *Magn Reson Med*. 2022;88(3):1419-1433. doi:10.1002/mrm.29288
- Zhang B, Seifert AC, Kim JW, Borrello J, Xu J. 7 Tesla 22-channel wrap-around coil array for cervical spinal cord and brainstem imaging. *Magn Reson Med*. 2017;78(4):1623-1634.
- Duan Q, Nair G, Gudino N, et al. A 7T spine array based on electric dipole transmitters. *Magn Reson Med*. 2015;74(4):1189-1197.
- Kraff O, Bitz AK, Kruszona S, et al. An eight-channel phased array RF coil for spine MR imaging at 7 T. *Invest Radiol*. 2009;44(11):734-740.
- Roemer PB, Edelstein WA, Hayes CE, Souza SP, Mueller OM. The NMR phased array. *Magn Reson Med*. 1990;16(2):192-225.
- Vossen M, Teeuwisse W, Reijnerse M, Collins CM, Smith NB, Webb AG. A radiofrequency coil configuration for imaging the human vertebral column at 7 T. *J Magn Reson*. 2011;208(2):291-297.
- Wu B, Wang C, Krug R, et al. 7T human spine imaging arrays with adjustable inductive decoupling. *IEEE Trans Biomed Eng*. 2010;57(2):397-403.
- Paška J, Cloos MA, Wiggins GC. A rigid, stand-off hybrid dipole, and birdcage coil array for 7 T body imaging. *Magn Reson Med*. 2018;80(2):822-832. doi:10.1002/mrm.27048
- Orzada S, Quick HH, Ladd ME, et al. A flexible 8-channel transmit/receive body coil for 7 T human imaging. In: Proc Intl Soc Mag Reson Med; 2009.
- Raaijmakers AJE, Italiaander M, Voogt IJ, et al. The fractionated dipole antenna: a new antenna for body imaging at 7 Tesla. *Magn Reson Med*. 2016;75(3):1366-1374.
- Rietsch SHG, Orzada S, Maderwald S, et al. 7T ultra-high field body MR imaging with an 8-channel transmit/32-channel receive radiofrequency coil array. *Med Phys*. 2018;45(7):2978-2990.
- Rietsch SHG, Brunheim S, Orzada S, et al. Development and evaluation of a 16-channel receive-only RF coil to improve 7T ultra-high field body MRI with focus on the spine. *Magn Reson Med*. 2019;82(2):796-810.
- Vaughan JT, Snyder CJ, DelaBarre LJ, et al. Whole-body imaging at 7T: preliminary results. *Magn Reson Med*. 2009;61(1):244-248.
- Moccia M, Ruggieri S, Ianniello A, Toosy A, Pozzilli C, Ciccarelli O. Advances in spinal cord imaging in multiple sclerosis. *Ther Adv Neurol Disord*. 2019;12:1756286419840593.
- Koning W, Bluemink JJ, Langenhuizen EAJ, et al. High-resolution MRI of the carotid arteries using a leaky waveguide transmitter and a high-density receive array at 7 T. *Magn Reson Med*. 2013;69(4):1186-1193.
- Massire A, Taso M, Besson P, Guye M, Ranjeva JP, Callot V. High-resolution multi-parametric quantitative magnetic resonance imaging of the human cervical spinal cord at 7T. *Neuroimage*. 2016;143:58-69.
- Pruessmann KP, Weiger M, Scheidegger MB, Boesiger P. SENSE: sensitivity encoding for fast MRI. *Magn Reson Med*. 1999;42(5):952-962.
- Sodickson DK, Manning WJ. Simultaneous acquisition of spatial harmonics (SMASH): fast imaging with radiofrequency coil arrays. *Magn Reson Med*. 1997;38(4):591-603.
- Wald LL, Wiggins GC, Potthast A, Wiggins CJ, Triantafyllou C. Design considerations and coil comparisons for 7 T brain imaging. *Appl Magn Reson*. 2005;29(1):19.
- Wiggins GC, Polimeni JR, Potthast A, Schmitt M, Alagappan V, Wald LL. 96-channel receive-only head coil for 3 Tesla: design optimization and evaluation. *Magn Reson Med*. 2009;62(3):754-762.
- Keil B, Biber S, Rehner R, et al. A 64-channel array coil for 3T head/neck/C-spine imaging. In: Proc Intl Soc Mag Reson Med; 2011.
- Wiesinger F, Van de Moortele PF, Adriany G, De Zanche N, Ugurbil K, Pruessmann KP. Parallel imaging performance as a function of field strength--an experimental investigation using electrodynamic scaling. *Magn Reson Med*. 2004;52(5):953-964.
- Van de Moortele PF, Akgun C, Adriany G, et al. B(1) destructive interferences and spatial phase patterns at 7 T with a head transceiver array coil. *Magn Reson Med*. 2005;54(6):1503-1518.



28. Ibrahim TS, Lee R, Baertlein BA, Abduljalil AM, Zhu H, Robitaille PM. Effect of RF coil excitation on field inhomogeneity at ultra high fields: a field optimized TEM resonator. *Magn Reson Imaging*. 2001;19(10):1339-1347.
29. Lattanzi R, Sodickson DK, Grant AK, Zhu Y. Electrodynamical constraints on homogeneity and radiofrequency power deposition in multiple coil excitations. *Magn Reson Med*. 2009;61(2):315-334.
30. Adriany G, Auerbach EJ, Snyder CJ, et al. A 32-channel lattice transmission line array for parallel transmit and receive MRI at 7 Tesla. *Magn Reson Med*. 2010;63(6):1478-1485.
31. Gilbert KM, Curtis AT, Gati JS, Klassen LM, Menon RS. A radiofrequency coil to facilitate  $B_1^+$  shimming and parallel imaging acceleration in three dimensions at 7 T. *NMR Biomed*. 2011;24(7):815-823.
32. Adriany G, Van de Moortele PF, Wiesinger F, et al. Transmit and receive transmission line arrays for 7 Tesla parallel imaging. *Magn Reson Med*. 2005; 53(2):434-445.
33. Mao W, Smith MB, Collins CM. Exploring the limits of RF shimming for high-field MRI of the human head. *Magn Reson Med*. 2006;56(4):918-922.
34. Katscher U, Börner P, Leussler C, van den Brink JS. Transmit SENSE. *Magn Reson Med*. 2003;49(1):144-150.
35. Henning A, Koning W, Fuchs A, et al. (1) H MRS in the human spinal cord at 7 T using a dielectric waveguide transmitter, RF shimming and a high density receive array. *NMR Biomed*. 2016;29(9):1231-1239.
36. Cui J, Dimitrov IE, Cheshkov S, Gu M, Malloy CR, Wright SM. An adjustable-length dipole using forced-current excitation for 7T MR. *IEEE Trans Biomed Eng*. 2018;65(10):2259-2266.
37. Duan Q, Sodickson DK, Lattanzi R, Zhang B, Wiggins GC. Optimizing 7T spine array design through offsetting of transmit and receive elements and quadrature excitation. In: Proc Intl Soc Mag Reson Med; 2010.
38. Graessl A, Langner S, Hoehne M, Dieringer MA, Niendorf T. En route to clinical ultrahigh field musculoskeletal MR using multi-purpose transceiver RF modules for spine and shoulder imaging at 7.0 T. *IEC*. 2006;60601:2-33.
39. Lakshmanan K, Cloos M, Brown R, Shepherd T, Wiggins GC. A four channel transmit receive "loopole" array for spine imaging at 7.0 Tesla. In: Proc Intl Soc Mag Reson Med; 2015.
40. Sigmund EE, Suero GA, Hu C, et al. High-resolution human cervical spinal cord imaging at 7 T. *NMR Biomed*. 2012;25(7):891-899.
41. Orzada S, Maderwald S, Kraff O, et al. 16-channel Tx/Rx body coil for RF shimming with selected  $C_p$  modes at 7T. In: Proc Intl Soc Mag Reson Med; 2010.
42. Orzada S, Solbach K, Gratz M, et al. A 32-channel parallel transmit system add-on for 7T MRI. *PLoS ONE*. 2019;14(9):e0222452.
43. Orzada S, Bahr A, Bolz T. A novel 7 T microstrip element using meanders to enhance decoupling. In: Proc Intl Soc Mag Reson Med; 2008.
44. Chen G, Cloos M, Lattanzi R, Sodickson DK, Wiggins GC. Bent electric dipoles: a novel coil design inspired by the ideal current pattern for central SNR at 7 Tesla. In: Proc Intl Soc Mag Reson Med; 2014.
45. Chen G, Sodickson D, Wiggins G. 3D curved electric dipole antenna for propagation delay compensation. In: Proc Intl Soc Mag Reson Med; 2015.
46. Chen G, Cloos M, Sodickson D, Wiggins G. A 7T 8 channel transmit-receive dipole array for head imaging: dipole element and coil evaluation. In: Proc Intl Soc Mag Reson Med; 2014.
47. Solomakha G, van Leeuwen C, Raaijmakers A, et al. The dual-mode dipole: a new array element for 7T body imaging with reduced SAR. *Magn Reson Med*. 2019;81(2):1459-1469.
48. Zivkovic I, de Castro CA, Webb A. Design and characterization of an eight-element passively fed meander-dipole array with improved specific absorption rate efficiency for 7 T body imaging. *NMR Biomed*. 2019;32(8):e4106.
49. Connell IRO, Menon RS. Shape optimization of an electric dipole array for 7 Tesla neuroimaging. *IEEE Trans Med Imaging*. 2019;38(9):2177-2187.
50. Avdievich NI, Solomakha G, Ruhm L, Scheffler K, Henning A. Evaluation of short folded dipole antennas as receive elements of ultra-high-field human head array. *Magn Reson Med*. 2019;82(2):811-824.
51. Clément JD, Gruetter R, Ipek Ö. A human cerebral and cerebellar 8-channel transceive RF dipole coil array at 7T. *Magn Reson Med*. 2019;81(2):1447-1458.
52. Clément J, Gruetter R, Ipek Ö. A combined 32-channel receive-loops/8-channel transmit-dipoles coil array for whole-brain MR imaging at 7T. *Magn Reson Med*. 2019;82(3):1229-1241.
53. Ertürk MA, Raaijmakers AJE, Adriany G, Uğurbil K, Metzger GJ. A 16-channel combined loop-dipole transceiver array for 7 Tesla body MRI. *Magn Reson Med*. 2017;77(2):884-894.
54. Eryaman Y, Guerin B, Keil B, et al. SAR reduction in 7T C-spine imaging using a "dark modes" transmit array strategy. *Magn Reson Med*. 2015;73(4): 1533-1539.
55. Lopez Rios N, Topfer R, Foias A, et al. Integrated AC/DC coil and dipole Tx array for 7T MRI of the spinal cord. In: Proc Intl Soc Mag Reson Med; 2019.
56. Gilbert KM, Klassen LM, Mashkovtsev A, Zeman P, Menon RS, Gati JS. Radiofrequency coil for routine ultra-high-field imaging with an unobstructed visual field. *NMR Biomed*. 2021;34(3):e4457.
57. Eichfelder G, Gebhardt M. Local specific absorption rate control for parallel transmission by virtual observation points. *Magn Reson Med*. 2011;66(5): 1468-1476.
58. Boulant N, Gras V, Amadon A, Luong M, Ferrand G, Vignaud A. Workflow proposal for defining SAR safety margins in parallel transmission. In: Proc Intl Soc Mag Reson Med; 2018.
59. Duan Q, Duyn JH, Gudino N, et al. Characterization of a dielectric phantom for high-field magnetic resonance imaging applications. *Med Phys*. 2014; 41(10):102303.
60. Hoffmann J, Henning A, Giapitzakis IA, et al. Safety testing and operational procedures for self-developed radiofrequency coils. *NMR Biomed*. 2016; 29(9):1131-1144.
61. International Electrotechnical Commission. Medical Electrical Equipment – Part 2-33: Particular Requirements for the Basic Safety and Essential Performance of Magnetic Resonance Equipment for Medical Diagnosis, Edition 3.1. International Electrotechnical Commission; 2013.
62. Kellman P, McVeigh ER. Image reconstruction in SNR units: a general method for SNR measurement. *Magn Reson Med*. 2005;54(6):1439-1447.
63. Chung S, Kim D, Breton E, Axel L. Rapid  $B_1^+$  mapping using a preconditioning RF pulse with TurboFLASH readout. *Magn Reson Med*. 2010;64(2): 439-446.

64. Marques JP, Kober T, Krueger G, van der Zwaag W, Van de Moortele PF, Gruetter R. MP2RAGE, a self bias-field corrected sequence for improved segmentation and T1-mapping at high field. *Neuroimage*. 2010;49(2):1271-1281.
65. De Leener B, Lévy S, Dupont SM, et al. SCT: spinal cord toolbox, an open-source software for processing spinal cord MRI data. *Neuroimage*. 2017; 145(Pt A):24-43.
66. D'astous A, Topfer R, Cereza G, et al. Shimming-toolbox: an open-source software package for performing realtime B0 shimming experiments. In: Proc Intl Soc Mag Reson Med; 2021; Online.
67. Rangaprakash D, Guerin B, Stockmann JP, et al. Performance characterization of three coils for whole brain and/or cervical spinal cord MRI at 7T. In: Proc Intl Soc Mag Reson Med; 2022.
68. Uğurbil K, Auerbach E, Moeller S, et al. Brain imaging with improved acceleration and SNR at 7 Tesla obtained with 64-channel receive array. *Magn Reson Med*. 2019;82(1):495-509.
69. Keil B. Construction of receive arrays. In: Proc Intl Soc Mag Reson Med; 2013.
70. Gras V, Vignaud A, Amadon A, Le Bihan D, Boulant N. Universal pulses: a new concept for calibration-free parallel transmission. *Magn Reson Med*. 2017;77(2):635-643.
71. Papp D, Boulant N, Massire A, Mauconduit F, Gras V, Cohen-Adad J. Universal pulses for the cervical spinal cord at 7T: a feasibility study. In: Proc Intl Soc Mag Reson Med; 2023.

## SUPPORTING INFORMATION

Additional supporting information can be found online in the Supporting Information section at the end of this article.

**How to cite this article:** Lopez-Rios N, Gilbert KM, Papp D, et al. An 8-channel Tx dipole and 20-channel Rx loop coil array for MRI of the cervical spinal cord at 7 Tesla. *NMR in Biomedicine*. 2023;e5002. doi:[10.1002/nbm.5002](https://doi.org/10.1002/nbm.5002)